Eur. Phys. J. C (2017) 77:506
DOI 10.1140/epjc/s10052-017-5068-2

THE EUROPEAN PHYSICAL JOURNAL C

Regular Article - Experimental Physics

The ν-cleus experiment: a gram-scale fiducial-volume cryogenic detector for the first detection of coherent neutrino–nucleus scattering

R. Strauss[1,a], J. Rothe[1], G. Angloher[1], A. Bento[2], A. Gütlein[3,4], D. Hauff[1], H. Kluck[3,4], M. Mancuso[1], L. Oberauer[5], F. Petricca[1], F. Pröbst[1], J. Schieck[3,4], S. Schönert[5], W. Seidel[1], L. Stodolsky[1]

[1] Max-Planck-Institut für Physik, 80805 Munich, Germany
[2] CIUC, Departamento de Fisica, Universidade de Coimbra, 3004 516 Coimbra, Portugal
[3] Institut für Hochenergiephysik der Österreichischen Akademie der Wissenschaften, 1050 Vienna, Austria
[4] Atominstitut, Vienna University of Technology, 1020 Vienna, Austria
[5] Physik-Department, Technische Universität München, 85748 Garching, Germany

Received: 26 April 2017 / Accepted: 14 July 2017 / Published online: 31 July 2017

Abstract We discuss a small-scale experiment, called ν-cleus, for the first detection of coherent neutrino–nucleus scattering by probing nuclear-recoil energies down to the 10 eV regime. The detector consists of low-threshold $CaWO_4$ and Al_2O_3 calorimeter arrays with a total mass of about 10 g and several cryogenic veto detectors operated at millikelvin temperatures. Realizing a fiducial volume and a multi-element target, the detector enables active discrimination of γ, neutron and surface backgrounds. A first prototype Al_2O_3 device, operated above ground in a setup without shielding, has achieved an energy threshold of ∼20 eV and further improvements are in reach. A sensitivity study for the detection of coherent neutrino scattering at nuclear power plants shows a unique discovery potential (5σ) within a measuring time of $\lesssim$2 weeks. Furthermore, a site at a thermal research reactor and the use of a radioactive neutrino source are investigated. With this technology, real-time monitoring of nuclear power plants is feasible.

1 Introduction

The detection of coherent neutrino–nucleus scattering (CNNS) is among the most challenging tasks of modern particle and astroparticle physics. A first observation of CNNS would be an important confirmation of the Standard Model of Particles and would open the door to new physics beyond the Standard Model (BSM).

Coherent neutrino–nucleus scattering (CNNS), first proposed in 1974 [1], is an unobserved neutral-current interaction predicted by the Standard Model of Particle Physics. Neutrino–nucleus scattering via Z_0-exchange becomes coherent over the nuclei at low transferred momenta, for large nuclei simultaneously boosting the interaction cross-section and reducing the recoil energies. The total elastic cross section for the process can be written as [2]

$$\frac{\mathrm{d}\sigma}{\mathrm{d}E_R} = \frac{G_\mathrm{F}^2}{8\pi(\hbar c)^4}((4\sin^2\theta_\mathrm{W} - 1)\cdot Z + N)^2 \cdot m_N \cdot (2 - E_R m_N/E_\nu^2)|f(q)|^2 \quad (1)$$

where G_F is Fermi's coupling constant, θ_W the Weinberg angle, Z, N and m_N are the nucleus' proton number, neutron number, and total mass, respectively, E_ν is the neutrino energy, and E_R the resulting nuclear-recoil energy. The nuclear form factor $f(q)$ describes the loss of coherence as a function of transferred momentum wavenumber $q = \sqrt{2m_N E_R}/\hbar$. It can be understood as the Fourier transform of the nuclear weak charge density, and is close to unity for small q (typically at $E_\nu \lesssim 50$ MeV).

The process remains unobserved until now due to the small recoil energies expected which challenge detector technologies. Multiple experimental efforts for detecting CNNS are made globally: the COHERENT experiment [3] which is currently taking data at the Spallation Neutron Source (SNS) uses a combination of conventional CsI, Ge and liquid-Xe detectors. Various other experiments are planned or being commissioned such as CONNIE [4] using CCDs [5], TEXONO [6] using ionization-based Ge detectors, and MINER [7] and RICOCHET [8] using cryogenic detector technology.

W. Seidel: Deceased 19 February 2017.

[a] e-mail: strauss@mpp.mpg.de

The ultra-low-threshold cryogenic calorimeters presented here (and in [9]) put a rapid detection of this process within reach technologically. The relatively large cross section compared e.g. to neutrino–electron scattering makes this experimental approach interesting in two ways: (1) CNNS is detectable with a small-scale experiment and a total target mass of 10 g within a measuring time of several weeks (see below), far less costly than traditional neutrino facilities. (2) A manageable scaling of the total target mass to the still moderate range of 1–10 kg opens up a new window for precision tests of neutrino properties and interactions beyond the standard model. A recent summary of CNNS sensitivity to BSM neutrino physics is given in [10], including the following potential observations.

- Interpreted within the standard model, a precise measurement of the CNNS cross-section allows one to determine the Weinberg angle at low-energy scale through Eq. (1). Transferred momenta in CNNS are on the order of few MeV/c^2, extending the reach of other planned low momentum-transfer precision experiments [11]. Together with knowledge on electroweak precision observables (e.g. from LEP), this allows one to probe the running of the Weinberg mixing angle [10] which is precisely predicted in the standard model [12]. This collective measurement has sensitivity to BSM contributions well above the LHC scale.
- The neutrino–quark sector of neutrino Non-Standard Interactions [13,14], i.e. modified V-A quark–neutrino couplings, may measurably modify the CNNS cross-section [10].
- Exotic Neutral Currents [10], i.e. general (pseudo-)scalar, (axial-)vector or tensor couplings can induce modifications in the CNNS cross section and energy spectrum.
- The possibility of observing active-to-sterile neutrino oscillations using CNNS is discussed in [15].
- For very low-energy thresholds, the magnetic moment of the neutrino (causing enhanced low-energy scattering with spin exchange) can be probed beyond current limits from neutrino–electron scattering [16].

2 The detector

2.1 A fiducial-volume cryogenic detector

A detector, sensitive to CNNS, faces two main challenges: an extremely low-energy threshold combined with extraordinarily small background levels. We present a new gram-scale cryogenic detector which combines the possibility of lowest nuclear-recoil thresholds ($\mathcal{O}(\lesssim 10$ eV)) and the advantages of a fiducial-volume device. Those provide active shielding by the outermost regions against external radiation which reduces the background level in the innermost target volume (the fiducial volume). Since an exact spatial position reconstruction of events is difficult to realize in thermal detectors, so far this potential could not be exploited.

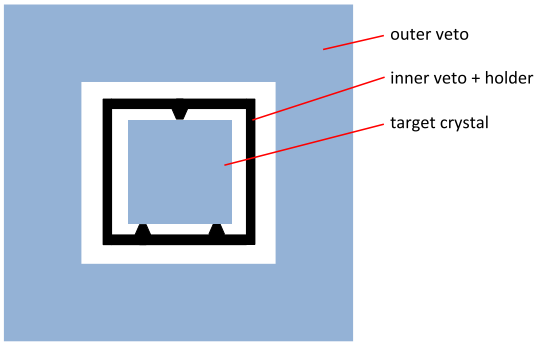

Fig. 1 Schematic view of the new detector which consists of three individual cryogenic calorimeters. The combination of, both, the outer veto against external gamma/neutron radiation, and the inner veto against surface alpha and beta decays, significantly reduces the background level in the target crystal. In this way, a fiducial-volume cryogenic detector is realized. The inner veto acts additionally as instrumented holder of the target crystal to reject possible stress-related relaxation events

Here, a cryogenic detector is presented which realizes a fiducial volume by combining three individual calorimeters: (1) a target crystal (the fiducial volume) with an extremely low threshold of $\mathcal{O}(\lesssim 10$ eV), (2) an inner veto as a 4π veto against surface beta and alpha decays, and (3) a massive outer veto against external gamma/neutron radiation (see Fig. 1). Additionally, the inner veto acts as an instrumented holder for the target crystal allowing to discriminate holder-related events (e.g. from stress relaxations).

2.2 Performance model for calorimeters

In order to design the new detector, a simple model was developed to predict the practically achievable performance of calorimeters of different geometry, material and mass [17]. The model is based on experimental results of cryogenic CRESST-type detectors. The main results are derived here, insofar as they drive design-choices for the fiducial-volume cryogenic detector.

The fundamental equation describing a calorimeter is that, for a system in internal thermal equilibrium, the temperature rise

$$\Delta T = \frac{\Delta E}{C} \tag{2}$$

where ΔE is an energy deposit and C is the heat capacity of the object. Reducing C yields a large increase in temperature and thus a high sensitivity to small energies.

Present cryogenic detectors of $\sim$300 g achieve energy thresholds of $\sim$300 eV [18]. In this work we investigate the performance and potential of gram-scale devices.

The fundamental energy resolution σ_E of cryogenic calorimeters is given by irreducible thermal fluctuations between the absorber and the thermal bath [19]:

$$\sigma_E^2 \sim k_B T^2 C \tag{3}$$

with the absorber's temperature T, heat capacity C and the Boltzmann constant k_B. This corresponds to theoretical energy resolutions of $\mathcal{O}(1\text{ eV})$ at $\sim$10 mK for massive calorimeters with masses of $\sim$100 g [20]. Phonon processes in cryogenic calorimeters with thin-film transition-edge-sensors (TESs) as considered in this work are well described by a dedicated thermal model [21].

Equation (2) is valid for a thermometer measuring the temperature of an absorber. In practice, the thermometers of cryogenic detectors can only measure their own temperature. Equation (2) thus changes to

$$\Delta T = E_{\text{abs}}/C_{\text{film}} \tag{4}$$

where E_{abs} denotes the energy absorbed in the thermometer and C_{film} the heat capacity of the thermometer film. In cryogenic calorimeters at very low temperatures ($\sim$10 mK), the energy deposition in the thermometer film happens via the absorption of non-thermal phonons, which propagate ballistically and interact directly with the metallic film electrons. Thus they are not affected by the weak thermal coupling between thermometer phonon and electron systems at such temperatures. To achieve sufficiently low heat capacities, temperatures as low as 10 mK are required for these devices. The strong electron–phonon decoupling in the thermometer film at these temperatures requires a dedicated thermal link to the heat bath. This strongly suppresses the thermal signal, which makes the non-thermal phonon component our dominant information carrier.

The thermometer's temperature rise can therefore be written as the ratio of the time-constants of the two competing processes that reduce the non-thermal phonon population: (1) the absorption in the thermometer with a time-constant τ_{film}, and (2) the thermalization of non-thermal phonons at the crystal surfaces with a time-constant τ_c

$$\Delta T = \frac{\tau_c}{\tau_{\text{film}}} \cdot \frac{\Delta E}{C_{\text{film}}}. \tag{5}$$

It should be noted that this is only valid in the limit $\tau_c \ll \tau_{\text{film}}$, which is equivalent to the statement that collection by the thermometer film does not influence the non-thermal phonon lifetime [21]. All devices considered here operate in this regime. Under these conditions, the temperature signal is not influenced by the presence of the thermometer, and thermometer optimization can be considered separately from a change in absorber parameters.

For the absorber scaling law, we keep only the quantities that depend on absorber properties. The energy threshold of the device is inversely proportional to the temperature rise, so we can write

$$E_{\text{th}} \propto \frac{\tau_{\text{film}}}{\tau_c}. \tag{6}$$

This is the basis for our scaling law which only considers varying absorber material, geometry and mass. Under these changes, τ_c scales with the average time between surface scatterings of the non-thermal phonons, which can be written

$$\tau_c \propto \frac{l}{\langle v_g \rangle} \tag{7}$$

in terms of the mean phonon free path in the crystal l and the mean phonon group velocity $\langle v_g \rangle$. For a fixed thermometer surface area, τ_{film} scales with the crystal volume and the mode-averaged absorption rate, like

$$\tau_{\text{film}} \propto \frac{V}{\langle v_\perp \alpha \rangle}. \tag{8}$$

$v_\perp \alpha$ is the volume spanned by the phonon modes that cross the thermometer surface per unit time and thermometer area, times the transmission probability into the thermometer. The different dimensionality, (i.e. l vs. V), in the scaling laws, arises from the fact that the crystal surface area scales up with the system dimensions, whereas the thermometer area does not.

In total, the scaling law is

$$E_{\text{th}} \propto \frac{V}{l} \cdot \frac{\langle v_g \rangle}{\langle v_\perp \alpha \rangle}. \tag{9}$$

The first part is purely geometric, while the second represents material parameters. The threshold of $CaWO_4$ detectors is expected to be 1.72 higher than Al_2O_3 of same geometry [17], while Si (1.42) and Ge (1.15) fall between these two. The scaling of two detector geometries as a function of mass are considered here. 1) For cubes of side length d, $V \propto d^3$ and $l \propto d$, so that $E_{\text{th}} \propto d^2$ which yields finally $E_{\text{th}} \propto m^{2/3}$. 2) For plates of area d^2 and fixed thickness h, $V \propto d^2$. In the relevant range, $10 \lesssim d/h \lesssim 100$, $l(d)$ rises slowly from $\sim 2h$ to $\sim 5h$ (from MC simulation). Roughly, we can take $l \approx$ const, which also gives $E_{\text{th}} \propto d^2$, but a different mass-scaling $E_{\text{th}} \propto m$.

With values for l found by Monte Carlo methods for each occurring detector geometry, the model can be used to describe the thresholds of various CRESST-type detectors. Since the model can only predict a scaling under change of absorber properties, the absolute normalization (depending e.g. on the noise level of the setup) has to be taken from the respective experiment. In the following, the noise level of the "benchmark" CRESST setup at LNGS is considered. In Fig. 2, the model predictions for plate and cube detectors are shown as a function of detector mass, fitted to the thresholds

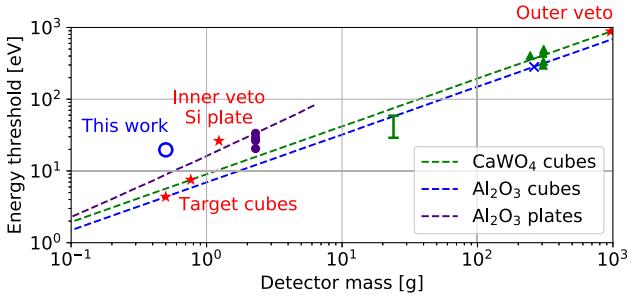

Fig. 2 Overview of the performance of different calorimeters: the nuclear-recoil energy threshold is plotted vs. the detector mass. The bands (1 σ) show predictions of the performance model for $CaWO_4$ (*green*) and Al_2O_3 (*blue*) calorimeters (see main text). The model is fitted to data of existing CRESST-type detectors (*green* and *blue*) [17,18,22–25]. *Red stars* indicate the predicted performance of the detector components studied in this work. The prediction bands for the new Si calorimeters are not shown for clarity

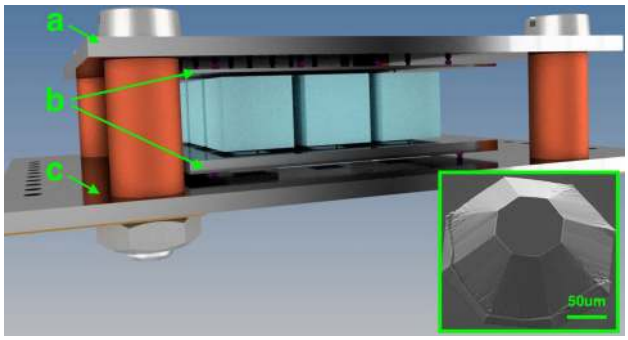

Fig. 3 Technical drawing of the calorimeter array. 3×3 cubic calorimeters (e.g. $CaWO_4$, Al_2O_3) are installed between two dedicated Si wafers (*b*). The contact area to the cubic crystals is realized by pyramides (height 200 μm) which are produced by wet chemical etching. The *inset* shows a microscopic picture of a prototype pyramidical structure. The outer Si wafers (*a*, *c*) act as holding structure and host the electrical wiring

achieved in CRESST-II $CaWO_4$ detectors (green triangles) with a mass of ∼300 g [18,22] and a sapphire cube of 262 g used in CRESST-I (blue cross) [23,24]. The model successfully predicts the energy threshold of CRESST-II light detectors studied in [17] (purple dots), which are sapphire discs with a mass of 2.2 g (diameter 40 mm, thickness 0.45 mm) and also the thresholds of ∼24 g CRESST-III detectors as expected from a prototype measurement (green error bar) [25]. The capability to extrapolate calorimeter thresholds for different detector geometries and materials over orders of magnitude in mass can be applied to the component design for the fiducial-volume cryogenic detector. Red stars indicate the calculated performance of the calorimeters studied here.

2.3 Design of the target calorimeter array

For the research program proposed in this work, the target calorimeter has to fulfill the following requirements:

- A nuclear-recoil energy threshold E_{th} of $\mathcal{O}(10\ \mathrm{eV})$.
- Rates of 10^2-10^3/[kg day] are expected from CNNS at the sites studied here, as will be shown in Sect. 3. Corresponding to this rate, a total target mass of ∼10 g is needed for the detection of CNNS.
- Lowest thresholds require a sufficiently low event rate in the calorimeter. To limit the pile-up contribution to a level of $\mathcal{O}(10^{-2})$, a maximum event rate of $\mathcal{O}(0.1\ \mathrm{Hz})$ per detector is allowed given the typical (thermal) pulse decay times of ∼100 ms [21].
- The CNNS cross-section is proportional to the target's neutron number N squared, which highly favors heavy elements. On the contrary, the use of light nuclei facilitates a characterization of neutron backgrounds.

Considering these design features, cubic target crystals with an edge length of 5 mm equipped with a tungsten thin-film TES are ideal. A multi-target approach with a variety of elements is chosen which has great advantages for the separation of signal and background through characteristic interaction strength. Cubes of $CaWO_4$ (0.76 g), Al_2O_3 (0.49 g), Ge and Si crystals, which are well-known for their excellent cryogenic detector properties [18,24], are suitable candidates. The performance model (see Sect. 2.2) predicts energy thresholds of $E_{\mathrm{th}} \approx 4.0$ eV for Al_2O_3 and $E_{\mathrm{th}} \approx 7.0$ eV for $CaWO_4$ (see red stars in Fig. 2). To obtain the desired total target mass, a 3 × 3 detector array is foreseen (see Fig. 3). This corresponds to a total target mass of 6.84 g for the $CaWO_4$ and 4.41 g for the Al_2O_3 array, respectively.

For the temperature sensor, a TES is chosen similar to that which is used for the CRESST detectors [25]. The TES consists of a thin W film (thickness 200 nm) with an area of 0.0061 mm^2 and an Al phonon collector with an area of 0.15 mm^2 attached to it (see Fig. 4). The latter increases the collection area for phonons without the penalty of increasing the heat capacity of the sensor [26] yielding an increased pulse height. The TES is weakly coupled to the heat sink via a thin Au stripe (0.01 × 7.0 mm^2, thickness 20 nm) providing a thermal conductance of ∼10 pW/K (at a temperature of 10 mK). Al and Au wire bonds with a diameter of 25 μm are used to provide the electrical contacts for the TES (bonded on the phonon collectors) as well as the ohmic heater (separate bond pads), and the thermal link to the heat sink, respectively. Typically, bias currents between 100 nA and 5 μA are applied to the sensor. The resistance change of the TES can be measured with a SQUID system similar to the one in the CRESST dark matter experiment [27].

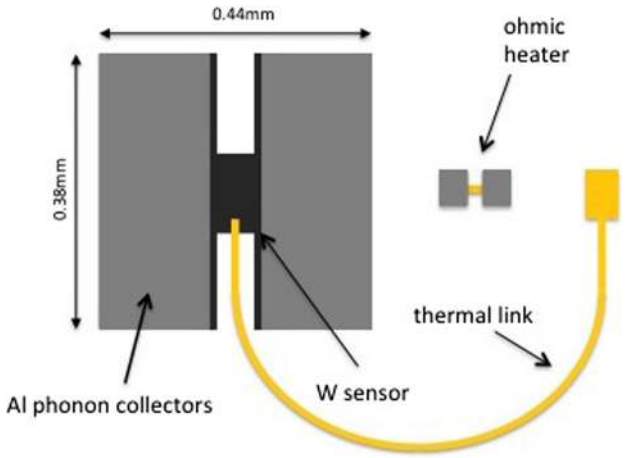

Fig. 4 Schematic view of the sensor design for the target calorimeter. A thin W film (thickness 200 nm) weakly coupled to the heat sink via a (0.01×7.0 mm^2 thickness 20 nm) Au stripe. An Al phonon collector is attached to the W film to increase the collection area of the sensor. The read-out current on the TES, the signals on the separate ohmic heater, and the thermal contact are connected via Al and Au wire bonds, respectively

2.4 Results from a prototype calorimeter

In the framework of this project, a prototype Al_2O_3 calorimeter of 0.5 g has been produced and equipped with a TES according to the design goals described in the previous section. The detector was installed in a copper holder and mounted in a detector test facility at the Max-Planck-Institut for physics in Munich. It consists of a dilution refrigerator in a surface building without dedicated shielding against ambient radioactivity. Further, no shielding against backgrounds from surfaces in the direct vicinity of the calorimeters is used. A ^{55}Fe X-ray source is placed close to the detector for a calibration of the low-energy region.

In an accompanying paper [9], we present details of a 5.1 h calibration measurement performed with the 0.5 g Al_2O_3 detector which achieved an energy threshold of $E_{\mathrm{th}} = (19.7 \pm 0.9)$ eV. This is independent of the type of particle interaction since it is a calorimetric device. This is the lowest nuclear-recoil energy threshold reported for massive calorimeters, beyond the fundamental nuclear-recoil reach of ionization-based detectors [28].

The detector operates in the calorimetric mode (see Sect. 2.2), confirmed by the pulse shape. The thermalization times in the crystal and thermometer film are found to be $\tau_c = 0.34$ ms and $\tau_{\mathrm{film}} = 2.2$ ms, respectively. This ratio fulfills the condition $\tau_c \ll \tau_{\mathrm{film}}$ but leaves room for improvements (see below).

The measured threshold is higher (by a factor of $\sim$5) compared to what is predicted by the performance model for calorimeters (Sect. 2.2). Part of the discrepancy may be explained due to worse noise level in the MPI setup (by factor 1.5–3 [25]) compared to the low-noise benchmark setup used for the calculation of the predictions (Eq. 9). The considered detector, being the first prototype of a gram-scale calorimeter, is expected to improve by further developments and adjustments of the TES sensor. The ratio of $\tau_c/\tau_{\mathrm{film}}$ can be further decreased by reducing the thermometer area and accordingly weakening the thermal link. A corresponding reduction of the Al phonon collectors may improve the transport efficiency of quasi-particles [26]. Furthermore, a moderate reduction of the W-film thickness will reduce the heat capacity of the thermometer without compromising the phonon absorption.

In the calibration measurement a flat background spectrum of $\sim 1.2 \times 10^5$ counts/[kg keV day] (7–10 keV) is observed above the calibration peaks [9]. This is expected due to the absence of any shielding and can be considered as an absolute upper limit for the total rate in surface experiments (here it corresponds to $\sim$0.3 Hz). It is comparable to typical total account rates observed in $\mathcal{O}$(1 kg) cryogenic detectors operated in underground laboratories [22]. The result clearly demonstrates that gram-scale detectors can be operated in a high-background environment – in particular at surface level – while allowing for low-energy thresholds and stable operating conditions.

The performance of the prototype fulfills the requirements listed in the previous section in terms of energy threshold and operability at surface level. To demonstrate the required background level – for the near future – measurements with further developed $CaWO_4$ and Al_2O_3 calorimeters at low-background experimental sites (e.g. a shallow laboratory) are planned. In particular, the target calorimeter(s) will be embedded in the inner and outer cryogenic shieldings which are discussed in detail in the following sections.

2.5 Low-threshold inner veto and detector holder

Background from the surfaces of the target crystals and surrounding surfaces is a big challenge for rare-event searches, and can limit the sensitivity at low energies. The inner veto provides an active discrimination against beta and alpha decays occurring on surfaces. Typical Q-values of such decays are between $\sim$10 keV and 10 MeV typically shared between 2,3 or more product particles leaving the interaction point in different directions. In a configuration where the target is surrounded by a 4π active veto, the total energy of the reaction is detected (apart from the energy transferred to neutrinos in beta decays). In this way, a high fraction of such backgrounds can be rejected by coincident events in the veto. The rejection of surface background is crucial in particular when approaching ultra-low-energy thresholds, as can be seen in experimental data (see e.g. [24]). Figure 5 shows a section view of the inner part of the detector. In the following, the functionality of the relevant detector components is briefly discussed.

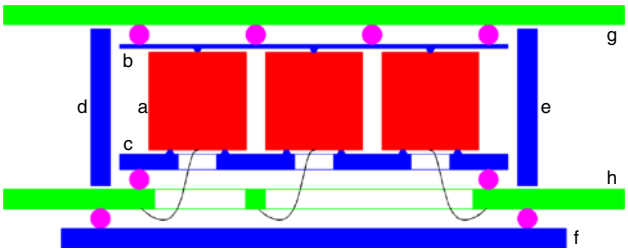

Fig. 5 Schematic side view of the detector array. *Red* Target calorimeter cubes (*a*) of (5 × 5 × 5) mm^3 with a TES each. *Blue* Si wafers instrumented with TESs providing a 4π surface veto (*b–f*). Two slabs have pyramides (*b*, *c*) with a height of 200 µm which are produced by wet chemical etching. These structure holds the target crystals. Slab *b* is flexible due to a thickness of only 200 µm. *Purple* Sapphire balls with a diameter of 1 mm. *Green* Two outer Si slabs (*g*, *h*) of 2 mm thickness press together the inner part. Slab *b* thereby acts as a spring. Slab *h* hosts the electrical wiring which is connected to the TES with wire bonds (*black*)

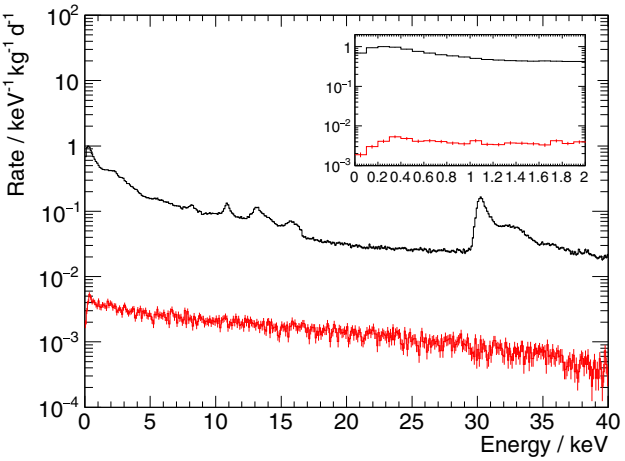

Fig. 6 MC simulation of the expected background from a contamination of the inner surface of the inner veto with a surface β-emitter (^{210}Pb). The *histograms* shows the energy deposits in the target for two cases: a passive inner veto (*black*) and an active inner veto (*red*) with a threshold of 30 eV. The *inset* zoom to the first 2 keV. Clearly a background reduction of $\mathcal{O}(10^2)$ is feasible at low energies

– Target (red): The detector consists of nine target calorimeters (a in Fig. 5) arranged in a 3 × 3 detector array. Each crystal is equipped with a TES (see Sect. 2.3).
– Active components (blue): To realize a 4π veto against surface backgrounds, Si wafers read-out by a TES each are used (b–f). Two of these (b and c) are in contact with the target crystals via pyramidal Si structures on the wafers. The upper one (b) is thin enough (200 µm) to be flexible – the wafer acts as a spring. Pressed to the target crystals, the thin wafer realizes a spring-loaded holding structure which can compensate for thermal contraction of the various components of the detector. Possible events induced by the detector holder (e.g. by thermal-stress relaxation) can be rejected since they induce also phonon signals in the TESs of b and c.
– Passive components (green): Two Si slabs (g and h) are used as support structures for the calorimeter array. They are attached to each other by 4 posts (shown in Fig. 3) providing the necessary pressure to hold the target crystals. The lower wafer (h) is equipped with Al (Au) wiring for the electrical (thermal) connection of the target calorimeters and the inner veto devices.

The inset in Fig. 3 shows a prototype Si wafer with a pyramid structure produced at the Halbleiterlabor of the Max-Planck-Society. The structure is defined by photolithography techniques and the pyramid structures are then realized by wet chemical etching.

The rejection power against surface related background was estimated with a dedicated Monte Carlo (MC) study performed with the Geant4 code in version 10.2p1 [29,30]. We follow the recommendation of the *Geant4 Low Energy Electromagnetic Physics Working Group* [31] and implement the low-energy behavior of electromagnetic interactions via the Geant4 class *G4EmStandardPhysics_option4*, a selection of most accurate models. Furthermore, we enabled the atomic de-excitation via emission of fluorescence photons and Auger electrons. With one exception, we applied a production cut of 250 eV throughout our geometry, i.e. for energies above this cut new secondary particles can be created in the simulation, whereas lower energies are directly deposited. The exception are fluorescence photons and Auger electrons which are produced in any case.

Being exemplary for surface contamination, we simulated the β-decay of ^{210}Pb by placing the lead ions at rest on the inner surface of the inner veto, facing one target calorimeter made of Al_2O_3. The source activity is assumed to be $\mathcal{O}(1\ \mathrm{kg}^{-1}\ \mathrm{keV}^{-1}\ \mathrm{day}^{-1})$, the maximal external β-activity observed with TUM40, a module with especially low background operated in CRESST-II phase 2 [32]. The black histogram in Fig. 6 shows the background spectrum seen by the target with inactive inner veto, the red histogram shows the spectrum of the remaining background in the case of an active veto with a threshold of 30 eV. Clearly a reduction of more than two orders of magnitude is feasible. A more detailed MC study of the complete detector array is under way and intended for future publication.

We note that the step at ∼100 eV (Fig. 6, *black histogram*) is no artifact of the used production cut. Instead, it is caused by Coster–Kronig transitions as part of the atomic relaxation subsequent to the decay of the 46.539 keV-level of ^{210}Bi to which ^{210}Pb decays in 84% of the cases [33].

2.6 Outer-veto detector

Given the smallness of the calorimeter array and the inner veto system, these components can be embedded in a large

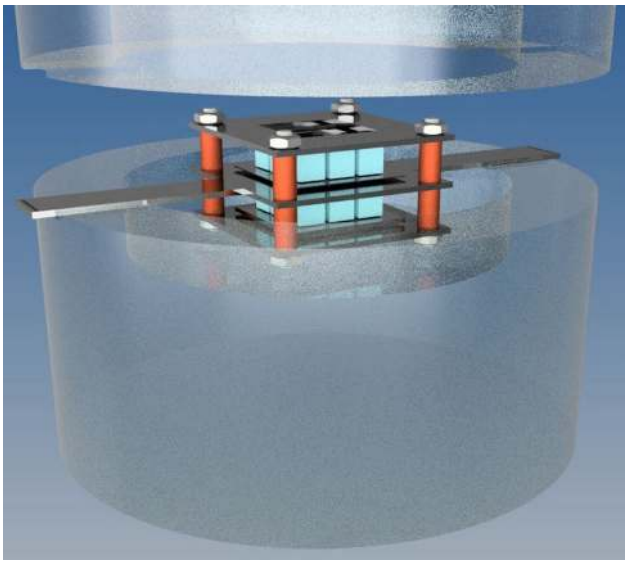

Fig. 7 Technical drawing of the fiducial-volume detector. Two calorimeter arrays are installed inside the $CaWO_4$ outer veto with diameter of 10 cm. The veto is made of two parts with a height of 5 cm each which are equipped with TESs and operated as cryogenic detectors

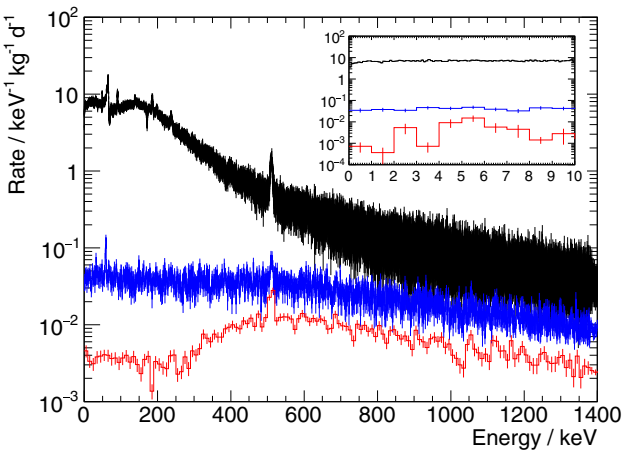

Fig. 8 MC simulation of the expected energy deposit in case of a γ-background similar to the remaining one in the Dortmund Low Background facility [35]. The *histograms* show the energy deposits in the target for three cases: without any veto (*black*), in the case of a passive outer veto (*blue*), and in the case of an active outer veto (*red*) with a threshold of 1 keV. The *inset* zoom to the first 10 keV. Clearly a background reduction of $\mathcal{O}(10^3)$ at lowest energies is reasonable

cryogenic outer veto. We consider cylindrical crystals with a diameter and height of $\mathcal{O}$(10 cm) which are segmented into two (or more) parts with a central cavity to host the inner detector parts (see Fig. 7). Each crystal of the outer veto is instrumented with a TES. It is foreseen to use materials that are known for their excellent phonon properties, such as e.g. Ge and $CaWO_4$, and that have been demonstrated as cryogenic detectors with masses of $\mathcal{O}$(100 g–1 kg). Thresholds between 300 eV and 1 keV are reached with such devices, in agreement with the prediction of the performance model for calorimeters in Sect. 2.2 (Fig. 2). $CaWO_4$ is the preferred material: it has the heavy element W which provides a high cross-section for gamma radiation and the relatively light element O for an efficient moderation of neutrons. The simulations below are therefore performed using $CaWO_4$. However, when scaling up the number of detectors (see Sect. 2.7) larger diameters of $CaWO_4$ crystals are necessary which currently are not available. In this case, Ge crystals are a promising alternative, since those are readily produced in large diameters (up to 300 mm), with high radiopurity.

It is worth mentioning that the timing information of pulses in the cryogenic detectors is crucial for the efficiency of a coincidence veto. The precision with which the onset of the pulses can be determined defines the dead time in the target calorimeter. We know from neutron scattering experiments that the pulse onset of comparable cryogenic calorimeters can be determined with a uncertainty of $\pm 5\,\mu$s [34]. Even an excessive rate of 100 Hz in the veto detector would introduce only a negligible dead time of $\lesssim 0.1\%$.

Also the rejection power of the outer veto was estimated with a MC study. Here a $CaWO_4$ target was placed inside the nested shields of inner and outer veto. As typical background we investigate gamma rays following the remaining spectrum at the Dortmund Low Background facility [35], a low-background site at the surface which will be discussed in Sect. 3. Figure 8 shows as black histogram the background spectrum observed by an unshielded target, in blue the remaining background in the case of a passive outer veto, and in red the remaining background in the case of an active outer veto with a threshold of 1 keV. Even with only a passive veto a background suppression of more than 3 orders of magnitude at low energies is feasible. Activating the outer veto increase the suppression to more than 4 orders of magnitude. Importantly, the expected gamma-induced electron-recoil spectrum remains flat down to energy threshold (see inset of Fig. 8).

For a first estimate of muon-induced neutron backgrounds, a basic MC simulation was performed. Using an active $CaWO_4$ outer veto, the neutron background is reduced by a factor of $\sim$10, independent of the recoil energy (studied in the energy range from 10 eV to 300 keV). By a clever combination of passive shielding elements like borated polyethylene, and active shielding elements like instrumented plastic or liquid scintillators, and LiF crystals, neutron background levels can be further reduced. This concerns shielding systems placed outside the cryogenic setup surrounding the cryostat at all sides. In addition we provide two technologies to further reduce and reject this potentially harmful background: (1) the outer cryogenic veto system described above and (2) the active background discrimination by the multi-target approach. The latter might be a powerful tool to reduce ulti-

mate backgrounds, particularly neutrons. This is described in more detail in Sect. 3. Nevertheless, we conclude that a dedicated MC simulation using measured muon spectra in combination with a calorimeter measurement at the experimental site are necessary. This is beyond the scope of this work and will be subject of a future publication.

2.7 Production and scalability

A disadvantage of cryogenic detectors when compared to e.g., scintillation detectors has always been the difficulty to scale up the experiments in size. The new detector concept presented here overcomes most of these problems. In principle, the detector has been designed such that the number of production steps of the individual detector components are independent of the number of target calorimeters involved.

The target calorimeters are produced from wafers with a thickness of 5 mm and variable diameters ($CaWO_4$ up to 60 mm, Al_2O_3 up to 200 mm, and Si up to 300 mm). With well-established techniques of the semiconductor industry, as e.g. photolithography, thin-film evaporation, etching or sputtering, the TES sensors are being simultaneously equipped on each target calorimeter, and the wafer is cut only afterwards into the individual $(5 \times 5 \times 5)$ mm^3 crystals. The same up-scaling is possible for the inner veto (Sect. 2.5) which acts as a detector holder. It is entirely produced by the above-mentioned methods. The cutting of the wafers is done by means of a laser or other automated methods. The cabling for a large amount of TES sensors are implemented by photolithography in combination with sputtering on the inner veto wafers as done for the 3×3 array. Further, it has been shown (e.g. in [36]) that large amounts of SQUIDs can be realized by SQUID multiplexing.

For the first phase of the experiment, we focus on the production of 3×3 arrays with moderate requirements of size and channel numbers which is foreseen as sufficient for a discovery of CNNS (see below). In a second step, the technology mentioned above enables experiments up to the kg-scale with energy thresholds of $\mathcal{O}(10\,\text{eV})$; an exposure allowing precision measurements of the CNNS cross-section and interesting BSM physics. Figure 9 shows a technical drawing of a future calorimeter array of 225 crystals which correspond, using Al_2O_3, to a total mass of $\sim$110 g.

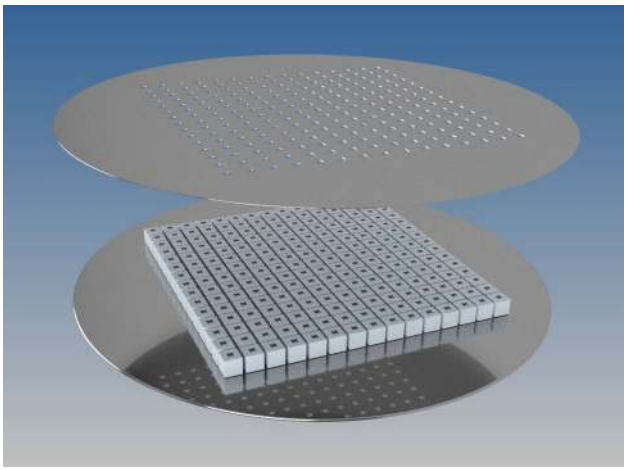

Fig. 9 Technical drawing of an up-scaled calorimeter array using state-of-the-art wafer sizes of 150 mm diameter (e.g. Al_2O_3 as target and Si as holder). In one production step, a total target mass of $\sim$110 g can be achieved using an array of 225 crystals

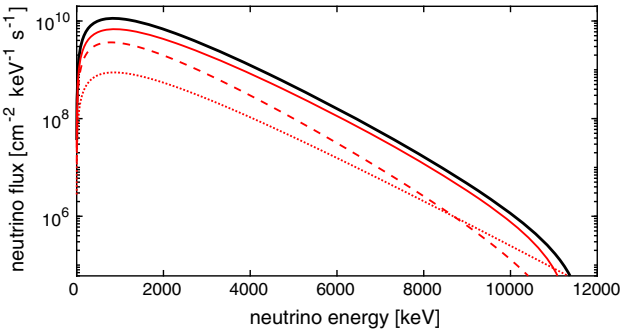

Fig. 10 Anti-neutrino flux from a benchmark pressurized-water nuclear reactor with a thermal power of 4 GW at a distance of 15 m. A standard fuel composition is used for the calculation: 62% of ^{235}U, 30% of ^{239}Pu and 8% of ^{238}U [38]

3 Detection of coherent neutrino scattering

3.1 Case 1: At a nuclear power reactor

3.1.1 Signal expectation

Nuclear power reactors are among the most intense (anti-) neutrino sources on earth and therefore a highly interesting site for the detection of CNNS.

A benchmark reactor with a thermal power of 4 GW, a typical value for a two-core reactor plant, yields $\sim 1.2 \times 10^{20}$ fissions per second and an isotropic neutrino rate of $R_\nu \approx 7.5 \times 10^{20}$ s^{-1} [37]. The neutrino flux $\Phi(E_\nu)$ can be calculated as

$$\Phi(E_\nu) = \frac{R_\nu}{4\pi d^2} \sum_i n_i \Phi_i(E_\nu) \tag{10}$$

with the distance to the core d, the fraction n_i of the fuel component i and the respective normalized neutrino-energy spectrum $\Phi_i(E_\nu)$. Figure 10 shows the neutrino flux for a standard fuel composition (62% of ^{235}U, 30% of ^{239}Pu and 8% of ^{238}U [38]) from a 4 GW reactor at a distance of $d =$ 15 m from the core.

The differential recoil spectrum in the detector can be written as

$$\frac{\mathrm{d}S}{\mathrm{d}E_R} = N_t \int_{E_{\min}}^{\infty} \frac{\mathrm{d}\sigma(E_\nu, E_R)}{\mathrm{d}E_R} \Phi(E_\nu) \mathrm{d}E_\nu \tag{11}$$

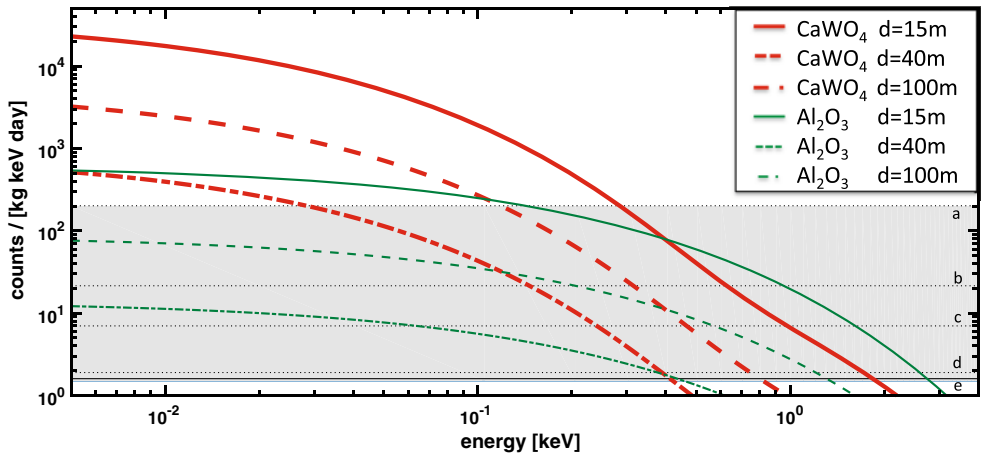

Fig. 11 Count rates on $CaWO_4$ (*red*) and Al_2O_3 (*green*) expected from a benchmark nuclear power plant of 4 GW for the three experimental sites considered. The *black dotted lines* indicate different background levels (extrapolation to lower energies) measured in different experimental sites. From *top to bottom*: *a* the Stanford shallow underground facility [39], *b* the low-background setup at the ARC in Seibersdorf [40], *c* the Dortmund low-background facility [35] and *d* the Heidelberg shallow laboratory [41]. The *full black line* (*e*) shows the expected (simulated) background level using the outer and inner veto of the fiducial-volume cryogenic detector. The *gray band* indicates the uncertainty of the background level with a lower limit at the intrinsic background level of $CaWO_4$ crystals measured at LNGS [32]. Reactor-correlated backgrounds are considered as negligible at the considered distances from core

using Eq. (1). N_t is the number of target nuclei and $E_{\min} = \sqrt{E_R M/2}$ the smallest neutrino energy leading to a recoil of a nucleus with the mass M.

The differential recoil spectra of coherently scattered antineutrinos in $CaWO_4$ and Al_2O_3 detectors at different distances d from the core of the benchmark reactor plant are shown in Fig. 11. Due to the N^2 dependency of the CNNS cross section (see Eq. 1), the heavy element W boosts significantly the rate on $CaWO_4$ below 100 eV (full red line) to $\sim 4 \times 10^4$ counts/[kg keV day]. The rate expected for Al_2O_3 (full green line), however, stays almost constant at a value of $\sim 1 \times 10^3$ counts/[kg keV day] below ~300 eV. The rates for $d = 40$ m are about a factor of 7 lower (dashed lines). The strong material dependence of the CNNS rate is a powerful tool to discriminate the signal from irreducible backgrounds. The signal rate is significantly different for $CaWO_4$ and Al_2O_3, e.g. at 10 eV the ratio is ~9.3. In contrast, the background counts from external gamma radiation is comparable (within a factor of ~2). Further, similar neutron background spectra are expected since in both materials - for neutron induced scatters - dominantly O scatters are above energy threshold due to kinematics.

The integrated count rates for different energy thresholds E_{th} and distances d are listed in Table 1. The signal is integrated up to an energy of 5 keV where the contribution to the signal is negligible. Count rates are given per day and kg as well as per day and detector array ($CaWO_4$: 6.84 g, Al_2O_3: 4.41 g). A signal rate of up to ~10 counts per array and day is expected for $CaWO_4$ target calorimeters.

Due to the relatively high rates predicted at such sites, the detection of CNNS with a small-scale detector of low threshold (~10 eV) at a moderate distance from the core is clearly in reach.

3.1.2 Background level

We consider a shallow experimental site with a small overburden to shield against cosmogenic backgrounds at $d \approx 15-100$ m from the reactor core. Possible candidate sites are, e.g., a room in the basement of a building outside the reactor containment, an artificial overburden outside the reactor building or even a site outside the reactor plant. At such places, the reactor-correlated gamma and neutron backgrounds are considered as negligible due to the large distance and significant shieldings. In the following we concentrate on uncorrelated backgrounds which at shallow sites are dominated by muon-induced events [35]. Plenty of experimental data describing detectors operated in shallow or above-ground low-background environments exist in the literature, mostly for Ge detectors. The following total background levels are reached in selected experiments: 0.4 counts/[kg keV day] at the shallow underground lab in Heidelberg [41], 5 counts/[kg keV day] at the Dortmund low-background facility [35], ~20 counts/[kg keV day] at the ARC in Seibersdorf [40] and 200 counts/[kg keV day] in the CDMS experiment operated at the Stanford underground facility [39] (black dotted lines). All values correspond to the rates in the lowest energy bin of the respective experiment. The gray band in Fig. 11 indicates the uncertainty in

Table 1 Integrated CNNS count rates from a nuclear reactor with a total thermal power of 4 GW at different distances d between E_{th} and 5 keV. The rates are integrated up to 5 keV

d [m]	E_{th} [eV]	Counts/[kg day]		Counts/[array day]	
		$CaWO_4$	Al_2O_3	$CaWO_4$	Al_2O_3
15	5	790.3	112.8	5.44	0.51
	10	690.2	110.1	4.75	0.49
	20	547.2	105.4	3.77	0.47
40	5	111.1	15.9	0.77	0.07
	10	97.1	15.5	0.67	0.07
	20	77.0	14.8	0.53	0.07
100	5	17.8	2.5	0.12	0.01
	10	15.5	2.5	0.11	0.01
	20	12.3	2.4	0.08	0.01

the observed background level depending on the individual site, the overburden and the shielding design. The lowest energy threshold (∼500 eV) among the listed experiments is achieved by CDMS [39].

We use the highest background level reported as a conservative upper limit for the sensitivity studies. Even more conservative, we do not consider the additional background-rejection capability of the inner and outer cryogenic veto. As shown in Sects. 2.5 and 2.6 by a dedicated MC study, the cryogenic fiducial-volume detector reduces surface, gamma and neutron backgrounds by factors of $\gtrsim 10^3$ and ∼10, respectively, in the target volume. In the following, the (flat) background rate of 200 counts/[kg keV day] is referred to as the benchmark.

In case of $CaWO_4$ the CNNS signal is 2–3 orders of magnitude above the conservative benchmark background whereas in the case of Al_2O_3 the signal-to-background ratio is much smaller (factor of 1–5); see Fig. 11. The multi-target approach, therefore, is a powerful tool to actively discriminate neutrino-induced signals from backgrounds. In particular, it allows one to identify possible ultimate exponentially shaped, signal-like backgrounds.

3.1.3 Experimental site and discovery potential

An extensive likelihood study is performed to investigate the discovery potential of CNNS with the proposed small-scale experiment. We consider one $CaWO_4$ (total mass: 6.84 g) and one Al_2O_3 (total mass: 4.41 g) calorimeter array inside the inner and outer active cryogenic veto (see Fig. 7). The benchmark background level is assumed and, conservatively, the rejection capability of the surface veto is not used for the background estimation. Three different thresholds are studied (5, 10 and 20 eV) which, however, have only a minor impact on the discovery potential. We define three scenarios:

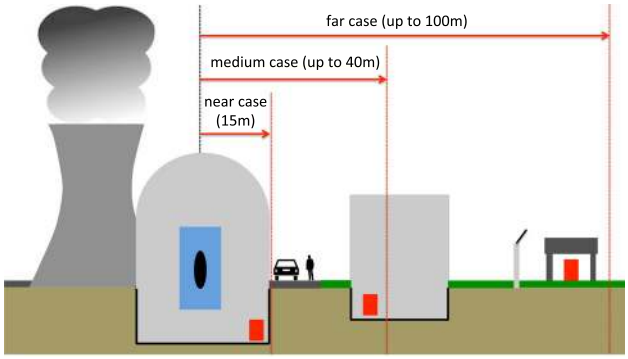

Fig. 12 Artist view of a typical nuclear power plant with possible experimental sites (*red boxes*) for the three different scenarios (see text)

- **Near case:** A distance of 15 m from the reactor core – a site within the reactor containment. Highest count rates are expected, but there are tough requirements for the shielding against correlated backgrounds. The access is restricted and strict safety regulations have to be considered.
- **Medium case:** A distance of 40 m from the reactor core – outside the containment and the reactor building. Possibly a shallow site in an adjoining building or a dedicated site with an artificial overburden. Easier access and a better infrastructure.
- **Far case:** A distance of 100 m from the reactor core – far away from the critical reactor components, possibly outside the entire power-plant area. Straightforward access and plenty of possible sites (Fig. 12).

For each case, spectra are randomly generated for a large number of varying exposures. The results of this MC simulation are studied with a likelihood ratio analysis. In every MC experiment, one spectrum each is generated for the $CaWO_4$ and Al_2O_3 arrays. The unbinned likelihood of a model's parameters is calculated as a product over the individual likelihoods for each event in both spectra and the Poisson likelihood for observing this total event number (Extended Maximum Likelihood method). The single event likelihood is proportional to the sum of the signal and background rates for the given parameter values. Two very simple models are considered: the free model has two parameters, namely the level of the flat background and the strength of the CNNS signal relative to the standard model expectation. In the null model, the CNNS signal strength is held at zero. The maximum likelihood of each model at the best fit parameter values is denoted $\mathcal{L}_{\text{free}}$ and $\mathcal{L}_{\text{null}}$ respectively. Since the two models are nested with one additional parameter in the free model, the likelihood ratio test statistic

$$W = 2 \log \frac{\mathcal{L}_{\text{free}}}{\mathcal{L}_{\text{null}}}$$

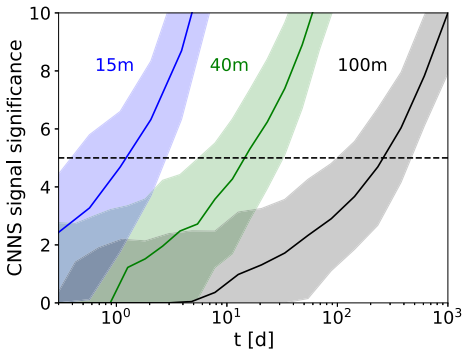

Fig. 13 Discovery potential of CNNS vs. time at a 4 GW reactor core from the likelihood ratio analysis described in the text. The combination of one $CaWO_4$ and one Al_2O_3 calorimeter array is investigated assuming the benchmark background level of 200 counts/[kg keV day]. The *full lines* indicate the median discovery probability for a nominal energy threshold of 10 eV, the bands show the 90% confidence intervals. Three cases for the reactor distance d are considered (see text): near case (*blue*), medium case (*green*) and far case (*gray*). Varying the threshold to 5 and 20 eV, respectively, has only a minor impact on the discovery potential (see text)

follows a χ^2-distribution with one degree of freedom (by Wilks' theorem). The square root of the test statistic therefore follows a standard normal distribution, so that the statistical significance in σ of the claim of a CNNS signal with nonzero cross-section in addition to the assumed flat background is directly given by $\sqrt{W}$ for each pair of spectra.

Figure 13 shows the resulting discovery potential of the three scenarios. The full lines indicate the median discovery potential as derived from the MC data, using an energy threshold of 10 eV. The bands give the 90% confidence intervals. All three scenarios show a very promising potential for the discovery (5σ) of CNNS – in the near case within $\sim$1 day, in the medium case within $\lesssim$2 weeks and in the far case within $\sim$1 year of measuring time. Improving the threshold to 5 eV reduces the measuring time necessary for a 5σ discovery by a factor of $\sim$1.3, in average for the three scenarios discussed. For a threshold of 20 eV, $\sim$1.6 times longer measurements are required.

Systematic deviations of background and signal rates have only minor influence on the discovery potential: Repeating the simulations with 20% higher and lower background level yield 10% higher and lower times to discovery, respectively. A 5% stronger signal makes discovery faster by 5%, while a 5% weaker signal requires 7.5% more measuring time.

To study the impact of a non-flat background on the discovery potential we use data from a CDMS detector operated at a shallow laboratory [39]. The measured spectrum was fitted with an exponential below 10 keV and extrapolated exponentially to beyond the energy threshold of 500 eV. The fitted background model corresponds to an exponential component rising above a flat background of 2.5 counts/[kg keV day] at around 2 keV and reaching 700 counts/[kg keV day] at zero energy. Using this background level in the likelihood study has only a minor impact. The measuring time required for a 5σ discovery in the three scenarios increase moderately by a factor of $\sim$2.5.

Background studies including dedicated measurements on the individual sites and detailed MC simulations are required to find the most suitable site. At the medium and far sites, expected backgrounds are rather straightforward, while for the near site a proper understanding of the possibly remaining reactor-correlated backgrounds is needed. The near site, however, would – despite a rapid discovery of CNNS – allow for a precision measurement (statistical error on a percent level) of the cross-section predicted by the Standard Model within a measuring time of one year. Impressively, this can be performed by a detector with a total target mass of $\sim$10 g, given the necessary control of systematics.

3.2 Case 2: At a thermal research reactor

To study the possibility of detecting CNNS at a thermal research reactor, both the signal and the background spectrum were adapted to the altered conditions. The signal expectation was calculated for the fuel composition found at FRM2 (96% of ^{235}U, 0% of ^{239}Pu and 4% of ^{238}U) [42] which does not change the signal shape appreciably. Our fiducial model is a 20 MW reactor at a distance of 3 m to the detector, which corresponds to a neutrino flux reduced by $\sim$2.4 with respect to the medium distance case at the power reactor. The close proximity to the research reactor implies great uncertainty regarding the composition and shape of backgrounds correlated to the reactor power, and thus to the neutrino signal. We use the results of a detailed background measurement and simulation campaign [7] by the MINER collaboration for our background estimate. In the framework of the MINER experiment it is planned to deploy an array of Ge cryogenic detectors in close proximity to a 1 MW research reactor [7]. Between the reactor core and the detectors, several layers of shielding made of graphite, borated high-density polyethylene, Pb and Cu are placed. These conditions are assumed to be comparable to the setup we are investigating in this context. Figure 14 shows the expected CNNS rates at the research reactor at a distance of 3 m from the core, along with the neutron (scaled to 10%; see below) and gamma backgrounds from [7]. Compared to those, cosmogenic backgrounds and environmental radioactivity appear to be sub-dominant in shallow labs (compare to Sect. 3.1.2) and are neglected in this basic feasibility study.

The similarity of the signal shape to the reactor-correlated neutron background makes the detection of CNNS challenging in this environment even with extensive reactor ON/OFF measurements. Under these conditions, a multi-target approach can be beneficial because of the material dependence of CNNS (since the cross-section is proportional

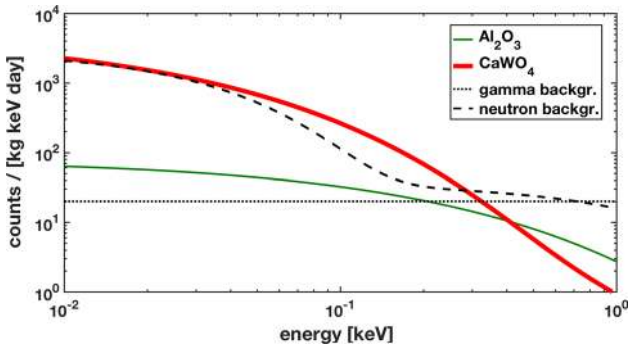

Fig. 14 Expected CNNS count rates at the FRM2 research reactor with a thermal power of 20 MW at a distance 3 m. The isotopic fractions of the neutrino emission is adjusted to 96% from ^{235}U and 4% from ^{238}U to account for the different fuel composition at FRM2. The *thick red* and *green lines* show the CNNS rates on $CaWO_4$ and Al_2O_3, respectively. In *black*, the simulated research-reactor background spectra for neutrons (scaled to 10%; see text) and gammas from [7] are shown

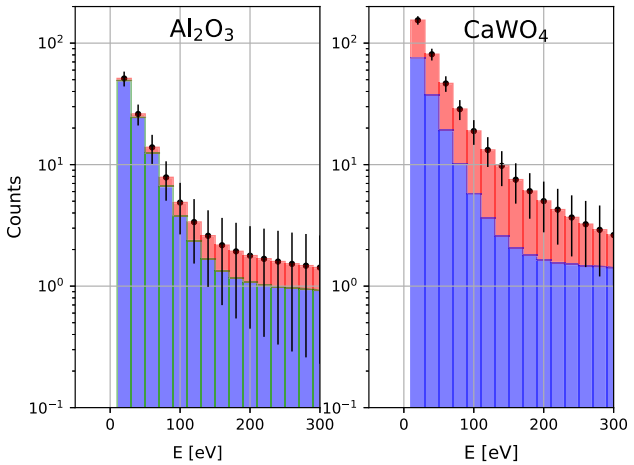

Fig. 15 Expected spectra at a thermal research reactor after 1 year of measurement in the Al_2O_3 array (*left*) and in the $CaWO_4$ array (*right*). Shown are the expected background counts (*blue*) from the MINER background scaled to 10%, and the expected CNNS signal counts (in *red*). The *error bars* show the expected fluctuations. The background spectra are assumed to be identical in the two materials, scaled only by the respective exposure (higher in $CaWO_4$ due to the higher density of the material). The CNNS signal is strongly enhanced in $CaWO_4$ due to the neutron-rich W nucleus. The Al_2O_3 array with a similar neutron response can serve for an in-situ background characterization

to N^2). In both $CaWO_4$ and Al_2O_3, neutrons are expected to scatter predominantly off the light oxygen nuclei, leaving a comparable signature. On the other hand, the Al_2O_3 array does not contribute meaningfully to the CNNS signal measurement, but yields an important measurement of the background rate as a function of energy. This information helps to break the degeneracy between the CNNS signal and the neutron background, which are very similar in shape.

Figure 15 shows the expected counts in the Al_2O_3 array (left) and in the $CaWO_4$ array (right) after one year of measurement in the described conditions. The similarity of the

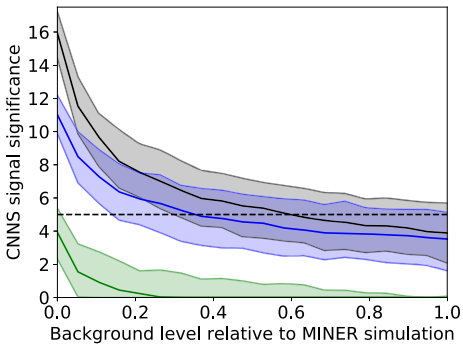

Fig. 16 CNNS discovery potential at a research reactor vs. background strength. The background is based on a detailed neutron simulation performed within the MINER collaboration (Fig. 14 in [7]). The detection significance is plotted separately for the Al_2O_3 (*green*) and $CaWO_4$ (*blue*) arrays. The combination of both (*black*) considerably enhances the detection significance. *Full lines* represent the median discovery potential, the *bands* constrained by thin lines are 90% confidence intervals as derived by the MC simulation

signal and background shapes in $CaWO_4$ is apparent. The signal in Al_2O_3 is overwhelmed by the Poisson fluctuations, so the Al_2O_3 array only contributes to the determination of the background level.

For the likelihood study, we assume a fixed live time of one year with the $CaWO_4$ and Al_2O_3 arrays and show the detection significance (computed as above) as a function of the background level instead. The simulated background spectrum is a scaled version of the MINER neutron background. The shape of the background spectrum is assumed to be known for the likelihood models. To show the added benefit of the Al_2O_3 array for background characterization, we plot the significance obtained by each detector material separately (green, blue) along with the combined significance (obtained as above, black) in Fig. 16. Full lines indicate the median discovery potential, the bands are 90% confidence intervals. The background level has to be reduced significantly with respect to the level reported in [7] to allow a 5σ-detection within one year. The "background-only" information provided by the Al_2O_3 array considerably relaxes the background requirements, so that a detection after one year becomes very likely with a background below $\sim$30% of the MINER neutron background, and feasible with a background below $\sim$60%.

3.3 Case 3: Using a neutrino source

The detection of CNNS using a radioactive neutrino source is a scenario which poses quite different challenges compared to the other considered cases. To evaluate the new situation, we assume a neutrino source similar to the source proposed for the SOX experiment [43], specifically we show in Fig. 17 the neutrino spectrum of a ^{144}Ce source with an initial activity of 150 kCi. The low-energy neutrinos ($\lesssim$300 keV) originate

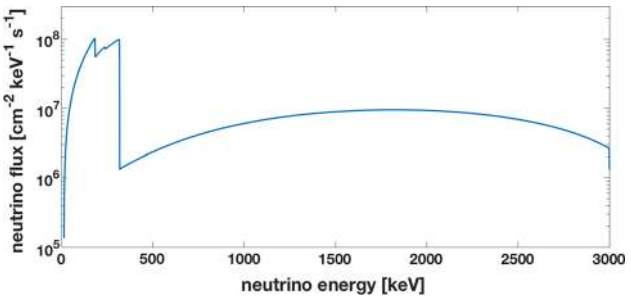

Fig. 17 Neutrino flux from the Ce neutrino source with an assumed activity of 150 kCi. The low-energy spectrum up to ∼300 keV corresponds to the initial ^{144}Ce decay, with the high-energy spectrum up to $Q = 3$ MeV stems from the decay of the daughter nucleus ^{144}Pr

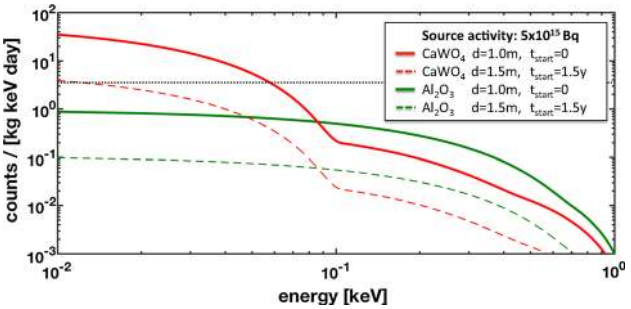

Fig. 18 Count rates expected from a benchmark ^{144}Ce neutrino source with an initial activity ($t_{\text{start}} = 0$) of 5×10^{15} Bq. The dotted lines indicate the worst-case scenario with a distance of 1.5 m and a measurement after two half-lifes of the source ($t_{\text{start}} = 1.5$ years). The *black dotted line* indicates the background level achieved with $CaWO_4$ in the CRESST setup at LNGS, Italy [32]

in the initial decay of ^{144}Ce with a half life of 285 days, while the broad neutrino spectrum up to a Q value about 3 MeV originates in the fast decay of the daughter nucleus ^{144}Pr. The low-energy neutrinos do not produce a detectable W recoil in the detectors considered here. With a 10 eV threshold, a $CaWO_4$ detector is sensitive mostly to neutrinos above 1 MeV. Therefore, even with an optimistic shielding scenario (source distance of 1 m) to stop residual gammas and neutrons from source impurities, the recoil rates are more than an order of magnitude below the far case of the power reactor scenario, as shown in Fig. 18.

The background level shown there is the measured intrinsic background of CRESST crystals, which constitutes the best reasonably achievable background level. We point out that any parasitic, radioactive contamination of the neutrino source which may produce additional neutron and gamma background is neglected in this study. With this optimistic assumption, detection of CNNS becomes feasible, but still suffers from low count rates.

Figure 19 shows the discovery potential of CNNS at 1 m from the benchmark radioactive neutrino source as a function of the exposure collected at full activity (150 kCi), obtained with the likelihood ratio method described above. Detection

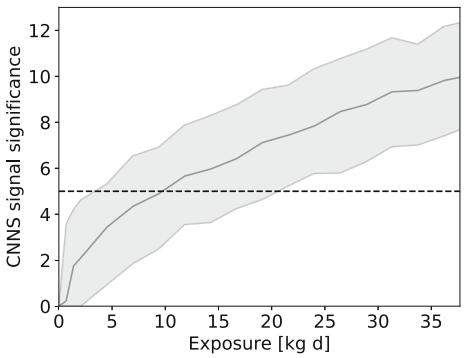

Fig. 19 Discovery potential of CNNS vs. exposure using a neutrino source, derived by a dedicated likelihood analysis. The *full line* represents the median discovery potential, the *band* is the 90% confidence interval. An exposure of ∼10 kg day is required for a detection of CNNS

comes in reach with an exposure of ∼10 kg day. Such exposures are feasible, however, they require a larger detector mass. The exposure has to be collected within a few half-lives of the source isotope ($t_{1/2} = 285$ days), which necessitates a larger array, e.g. 10×10 cubes (∼50 g).

4 Summary and outlook

The smallness of gram-scale calorimeters offers the following significant advantages: (1) very low-energy thresholds down to the 10 eV regime and presumably below, (2) the possibility of an encapsulation of the small calorimeters by other cryogenic devices which act as anti-coincidence vetos and (3) the ability to operate the detectors at the surface in a relatively high-rate environment. These advantages are demonstrated experimentally by a measurement with a prototype 0.5 g Al_2O_3 calorimeter which reaches a threshold of ∼20 eV. Based on that, we propose a new detector concept here: a gram-scale fiducial-volume cryogenic detector for the detection of CNNS, called the ν-cleus experiment.

A basic version of the detector, consisting of two 3×3 calorimeter arrays made of $CaWO_4$ and Al_2O_3 crystals with a total mass of ∼10 g, has a high potential for a rapid discovery of CNNS. We study various experimental scenarios for this new technology: an installation at a nuclear power plant, at a thermal research reactor and close to a radioactive neutrino source. We conclude that all three methods allow a detection of CNNS, however, the first scenario clearly shows the highest potential.

We investigate the operation of the 10 g detector at a distance of ∼40 m from a nuclear power reactor with a thermal power of 4 GW. This corresponds to an experimental site outside the reactor containment, and is therefore rather straightforward in terms of background levels, infrastructure

and access. As shown by a dedicated likelihood analysis, the rate is still sufficiently high to achieve a 5σ discovery within a measuring time of $\lesssim$2 weeks.

The detector placed at a well-shielded site within the reactor containment, e.g. at a distance of $\sim$15 m from the core, would give the unique possibility for precision measurements of the CNNS cross-section and probe, e.g. the Weinberg angle at low momentum transfers [10]. Furthermore, since a discovery of CNNS is possible within a day, this technology can be used for real-time monitoring of nuclear reactors. Such a small-scale experimental setup could provide a comprehensive surveillance system for non-proliferation and accident prevention at the $\sim$500 nuclear reactors world-wide.

The detector is designed such to be scaled up in a relatively simple way due to the use of production techniques of the semiconductor industry. We point out that total target masses of $\mathcal{O}$(1 kg) are feasible with the design principle given here. This enables new approaches in rare events searches, such as the search for MeV-scale dark matter and flavor-independent precision measurements of the solar neutrino flux. Operating such a kg-scale detector with energy thresholds in the 10 eV regime at a power reactor opens the door to a variety of new physics beyond the Standard Model of Particle physics.

Funded by SCOAP[3].

References

1. D.Z. Freedman, Phys. Rev. D **9**, 1389 (1974)
2. A. Drukier, L. Stodolsky, Phys. Rev. D **30**, 2295 (1984)
3. D. Akimov et al. (2015). arXiv:1509.08702
4. A. Aguilar-Arevalo et al., J. Phys. Conf. Ser. **761**(1), 012057 (2016). doi:10.1088/1742-6596/761/1/012057
5. G. Fernandez Moroni, J. Estrada, E.E. Paolini, G. Cancelo, J. Tiffenberg, J. Molina, Phys. Rev. D **91**(7), 072001 (2015). doi:10.1103/PhysRevD.91.072001
6. S. Kerman, V. Sharma, M. Deniz, H.T. Wong, J.W. Chen, H.B. Li, S.T. Lin, C.P. Liu, Q. Yue, Phys. Rev. D **93**(11), 113006 (2016). doi:10.1103/PhysRevD.93.113006
7. G. Agnolet et al., Nucl. Instrum. Methods A **853**, 53–60 (2017). http://adsabs.harvard.edu/abs/2016. arXiv:1609.02066
8. J. Billard et al. (2016). arXiv:1612.09035
9. R. Strauss et al., (2017). https://inspirehep.net/record/1591648. arXiv:1704.04317
10. M. Lindner, W. Rodejohann, X.J. Xu, JHEP **1703**, 097 (2017). arXiv:1612.04150
11. N. Berger et al., J. Univ. Sci. Tech. China **46**(6), 481–487 (2016). http://adsabs.harvard.edu/abs/2015. arXiv:1511.03934
12. J. Erler, M.J. Ramsey-Musolf, Phys. Rev. D **72**, 073003 (2005)
13. T. Ohlsson, Rep. Prog. Phys. **76**(4), 044201 (2013)
14. A. Santamaria, C. Peña Garay, S. Davidson, N. Rius Dionis, J. High Energy Phys. **0303**, 011 (2003)
15. A.J. Anderson et al., Phys. Rev. D **86**, 013004 (2012)
16. H.T. Wong et al., Mod. Phys. Lett. A **20**(15), 1103 (2005)
17. J. Rothe, Master's thesis, LMU München (2016). https://publications.mppmu.mpg.de (MPP-2016-391)
18. G. Angloher et al., Eur. Phys. J. C **76**(1), 25 (2016)
19. S.H. Moseley et al., J. Appl. Phys. **56**(5), 1257 (1984)
20. M. Pyle, E. Figueroa-Feliciano, B. Sadoulet (2015). http://adsabs.harvard.edu/abs/2015. arXiv:1503.01200
21. F. Pröbst et al., J. Low Temp. Phys. **100**(1–2), 69 (1995)
22. G. Angloher et al., Eur. Phys. J. C **74**(12), 3184 (2014)
23. O. Meier et al., Nucl. Instrum. Methods A **444**, 350 (2000)
24. G. Angloher et al., Astropart. Phys. **18**(1), 43 (2002)
25. R. Strauss et al., Nucl. Instrum. Methods A **845**, 414 (2017)
26. G. Angloher et al., J. Low Temp. Phys. **184**(1), 323 (2016)
27. G. Angloher et al., Eur. Phys. J. C **72**, 1971 (2012)
28. R. Agnese et al., Phys. Rev. D **95**, 082002 (2017)
29. S. Agostinelli et al., Nucl. Instrum. Methods A **506**(3), 250 (2003). doi:10.1016/S0168-9002(03)01368-8
30. J. Allison et al., IEEE Trans. Nuclear Sci. **53**(1), 270 (2006). doi:10.1109/TNS.2006.869826
31. Geant4 Low Energy Electromagnetic Physics Working Group. Low energy physics lists (2016). https://twiki.cern.ch/twiki/bin/view/Geant4/LowePhysicsLists
32. R. Strauss et al., JCAP **1506**(06), 030 (2015)
33. R.B. Firestone, *Table of Isotopes*, 8th edn. (Wiley, New York, 1996)
34. R. Strauss et al., Eur. Phys. J. C **74**(7), 2957 (2014). doi:10.1140/epjc/s10052-014-2957-5
35. H. Gastrich et al., Appl. Radiat. Isot. **112**, 165 (2016)
36. M.A. Dobbs et al., Rev. Sci. Instrum. **83**(7), 073113 (2012)
37. V. Kopeikin, L. Mikaelyan, V. Sinev, Phys. Atom. Nucl. **67**, 1892 (2004) [Yad. Fiz. **67**, 1916 (2004)]
38. O. Tengblad et al., Nucl. Phys. A **503**, 136 (1989)
39. D.S. Akerib et al., Phys. Rev. D **82**, 122004 (2010)
40. M. Schwaiger, F. Steger, T. Schroettner, C. Schmitzer, Appl. Radiat. Isot. **56**(1–2), 375 (2002). doi:10.1016/S0969-8043(01)00217-2
41. G. Heusser et al., Eur. Phys. J. C **75**(11), 531 (2015)
42. J. Wuttke et al., Rev. Sci. Instrum. **83**(7), 075109 (2012). doi:10.1063/1.4732806
43. M. Vivier et al., J. Phys. Conf. Ser. **718**(6), 062066 (2016)